Rapid #: -7895989

CROSS REF ID: **1096304**

LENDER: **GSU :: Main Library**

BORROWER: **UUM :: Marriott Library**

TYPE:	Article CC:CCG
JOURNAL TITLE:	Pure and applied geophysics
USER JOURNAL TITLE:	Pure and Applied Geophysics
ARTICLE TITLE:	Numerical Modeling of Ice Fog in Interior Alaska Using the Weather Research and Forecasting Model
ARTICLE AUTHOR:	Chang Ki Kim, Martin Stuefer, Carl G. Schmitt, And
VOLUME:	NA
ISSUE:	NA
MONTH:	January
YEAR:	2014
PAGES:	1-20
ISSN:	0033-4553
OCLC #:	

Pure Appl. Geophys.

DOI 10.1007/s00024-013-0766-7

Pure and Applied Geophysics

Numerical Modeling of Ice Fog in Interior Alaska Using the Weather Research and Forecasting Model

Chang Ki Kim,[1,3] Martin Stuefer,[1] Carl G. Schmitt,[2] Andrew Heymsfield,[2] and Greg Thompson[2]

Abstract—An ice microphysics parameterization scheme has been modified to better describe and understand ice fog formation. The modeling effort is based on observations in the Sub-Arctic Region of Interior Alaska, where ice fog occurs frequently during the cold season due to abundant water vapor sources and strong inversions existing near the surface at extremely low air temperatures. The microphysical characteristics of ice fog are different from those of other ice clouds, implying that the microphysical processes of ice should be changed in order to generate ice fog particles. Ice fog microphysical characteristics were derived with the NCAR Video Ice Particle Sampler during strong ice fog cases in the vicinity of Fairbanks, Alaska, in January and February 2012. To improve the prediction of ice fog in the Weather Research and Forecasting model, observational data were used to change particle size distribution properties and gravitational settling rates, as well as to implement a homogeneous freezing process. The newly implemented homogeneous freezing process compliments the existing heterogeneous freezing scheme and generates a higher number concentration of ice crystals than the original Thompson scheme. The size distribution of ice crystals is changed into a Gamma distribution with the shape factor of 2.0, using the observed size distribution. Furthermore, gravitational settling rates are reduced for the ice crystals since the crystals in ice fog do not precipitate in a similar manner when compared to the ice crystals of cirrus clouds. The slow terminal velocity plays a role in increasing the time scale for the ice crystals to settle to the surface. Sensitivity tests contribute to understanding the effects of water vapor emissions as an anthropogenic source on the formation of ice fog.

Key words: Ice fog, Homogeneous freezing, Haze droplets, Gamma distribution, WRF.

Abbreviations and Symbols

a_{r_i}	7.22
b_{r_i}	–0.35
$a_{w,liq}$	Water activity of solution in liquid phase
Δa_w	Difference of water activity between liquid and ice
D	Diameter for an individual ice crystal
HPP	Heat and power plant
IWC	Ice water content
J_h	Nucleation rate of haze droplets
J_s	Nucleation rate of pure water
M	Molality of solution
M_w	Molecular weight of pure water
MOD	Experiment with modified Thompson scheme
MODIS	Moderate resolution imaging spectroradiometer
MSLP	Mean sea level pressure
MWMD	Mass-weighted mean diameter
NARR	North American Regional Reanalysis
NCEP	National Center for Environment Prediction
NOE	Experiment without water vapor emission
N_c	Number concentration of cloud droplets
$N_{f,h}$	Number concentration of haze droplets freezing in time step
$N_{f,s}$	Number concentration of cloud droplets freezing in time step
N_h	Number concentration of haze droplets
N_i	Number concentration of ice crystals
$n(D)$	Size distribution
OBS	Observation
ORG	Experiment with original Thompson scheme
q_{ve}	Water vapor mixing ratio emitted from the source
q_v	Water vapor mixing ratio

[1] Geophysical Institute, University of Alaska Fairbanks, Fairbanks, AK, USA.

[2] National Center for Atmospheric Research, Boulder, CO, USA.

[3] *Present Address*: Department of Atmospheric Sciences, University of Arizona, 1118 E 4th Street, Tucson, AZ 85721-0081, USA. E-mail: ckkim@atmo.arizona.edu

Published online: 18 January 2014

RAMS	Regional atmospheric modeling system
RH	Relative humidity
RRTMG	Rapid Radiative Transfer Model for GCM application
r_h	Radius of haze droplet
SUCCESS	SUbsonic aircraft: Contrail and Cloud Effects Special Study
T	Air temperature
VIPS	Video ice particle sampler
V_l	The volume of droplets
V_h	The volume of haze droplet
v_t	Terminal velocity of ice crystal
WRF	Weather research and forecasting
YSU	Yonsei University
α	0.647×10^7
β	1.73
Φ_s	Molal osmotic coefficient
λ	Scale factor
μ	Shape factor
θ_e	Equivalent potential temperature
υ	Dissociation constant for solute

1. Introduction

Alaska is typically thought of as a large region with a sparse population and clean air, and in general this concept is acceptable. However, the air quality of some populated areas in Interior Alaska repeatedly exceeds the National U.S. Ambient Air Quality Standards in the winter. Besides anthropogenic air pollution through combustion products from industry, housing, and mobile sources, there is also frequent visibility degradation due to ice fog in Interior Alaska during the cold seasons. Ice fog is defined as tiny ice crystals near the ground surface (THUMAN and ROBINSON 1954) and it is produced frequently when the air is cold enough for ice nuclei to be activated or homogeneous ice nucleation to occur when sufficient water vapor is available (BENSON 1970). HUFFMAN and OHTAKE (1971) emphasized that ice fog particles should be distinguished from 'ice crystals', which are the product of nucleation and growth at higher altitude.

The region of Fairbanks, Alaska, is prone to ice fog formation because water vapor is emitted sufficiently from anthropogenic sources and the air temperature (T) is often below −40 °C during winter (HUFFMAN and OHTAKE 1971). In the first detailed study of ice fog, THUMAN and ROBINSON (1954) found that the mean ice crystal diameter decreases as T decreases; they found that at −40 °C, the mean diameter of the irregular-shaped particles, referred to as droxtal–faceted quasi-spherical particles, is 13 μm. KUMAI (1966) reported that most ice fog particles are between 2 and 15 μm in diameter with a sharp peak in the distribution near 7 μm, and that the number concentration of ice crystals (N_i) is between 100 and 200 cm^{-3}. Note that the unit of N_i is cm^{-3}, not L^{-1}. Typically, N_i during ice fog is much higher than N_i observed in the cirrus clouds of the mid-latitudes (e.g., ROGERS and YAU 1989; PRUPPACHER and KLETT 1997) and even in other Arctic clouds (e.g., CURRY *et al.* 1990, 2000; BIGG 1996; PRENNI *et al.* 2007, 2009). For example, PRENNI *et al.* (2009) reported an average N_i of <1 L^{-1} for Arctic clouds. GULTEPE *et al.* (2013) carried out an intensive field experiment as a part of FRAM-ICE. They examined that N_i is higher than 1 cm^{-3}. Our analysis (SCHMITT *et al.* 2013) shows an N_i that is comparable to typical number concentrations of warm fog droplets (171–604 cm^{-3}, KUNKEL 1984), implying that ice fog particles are deeply related to the fog droplets that are freezing homogeneously. The large difference of N_i between ice fog and Arctic clouds may be due to the mode of formation through anthropogenic activities (e.g., car exhaust, power plant cooling ponds), as well as the local meteorological characteristics.

The study by BENSON (1970) demonstrated the importance of anthropogenic activities for the formation of ice fog. He suggested the optimized conditions necessary to form ice fog: (1) a temperature T lower than −40 °C, (2) a strong inversion near the ground, (3) water vapor emissions, and (4) the presence of inactivated haze droplets. The first two conditions are related to the local meteorological characteristics. The climatological mean January T in Fairbanks is −23 °C, and the average number of January days with the minimum T lower than −29 and −40 °C are 13 and 5, respectively (SHULSKI and WENDLER 2007). Strong inversions form as a consequence of polar anticyclones and the negative heat balance at the surface due to the outgoing longwave radiation under the frequent clear skies during near polar light conditions. In addition, weak horizontal pressure gradients and topographic features support persistent periods with low winds, preventing

horizontal exchange processes. Inversions in the vicinity of Fairbanks are strong and persistent. BENSON (1970) reported that the vertical gradient of T typically reached 30 °C $(100\ \text{m})^{-1}$ within an altitude range from the surface to 50–100 m. The latter two ice fog conditions of water vapor emissions and an abundance of inactivated haze droplets correspond to the anthropogenic sources. An abundance of water vapor results as a combustion byproduct from cars and power plants in Fairbanks. BENSON (1970) calculated that Fairbanks has a water vapor release rate of 4×10^6 kg day^{-1}. In general, the influence of water vapor emissions from cars and power plants on meteorological conditions is weak in the other urban areas outside the Arctic and Subarctic. Since the saturation vapor pressure at −40 °C is 255 times lower than that at 15 °C, water vapor emissions from anthropogenic sources can play a crucial role in forming ice fog with decreasing temperatures. In addition to water vapor emission, water vapor itself is condensed on cloud condensation nuclei as an inactivated haze droplet. SHAW (1983) observed that the mean number concentration of haze droplets ranges from 170 to 2,000 cm^{-3} in Interior Alaska during mid-winter. CHEN *et al.* (2000) demonstrated through laboratory experiments that ice particles can be formed by the homogeneous freezing of haze droplets, which are nucleated on ammonium sulfate at high relative humidity (RH) and low T. Thus, because of the effects of anthropogenic activities on the formation of ice fog, BENSON (1970) referred to ice fog as local air pollution and emphasized the understanding of the local characteristics of ice fog.

Meanwhile, there are few studies on the formation of ice fog through numerical simulations. HUFFMAN and OHTAKE (1971) developed the theoretical equations to quantify the evolution of the size distribution of ice fog particles. Recently, a series of studies by GIRARD and BLANCHET (2001a, b) showed that aerosols and ice crystals can be generated by the authors' explicit aerosol-cloud-radiation model with sophisticated bin microphysics. These previous studies used simple theoretical models and idealized cases. More recently, ZHOU (2011) has developed a diagnostic approach to forecast the ice fog episode with an operational modeling output. However, a prognostic approach in the used three-dimensional mesoscale modeling work would be essential in order to better understand the nature of ice fog. GULTEPE *et al.* (2013) pointed out that current mesoscale models predict an N_i of $<100\ \text{L}^{-1}$ by the microphysical parameterization optimized to the general weather condition. The authors state that the microphysical processes need to be adjusted for the specific environment of ice fog. As a consequence, we explicitly implemented the homogeneous freezing processes into the mesoscale numerical model in order to better describe and assess the formation of ice fog. In this context, we also want to point out that our observed and modeled ice fog microphysics are very similar to the microphysics found in aircraft condensation trails (contrails) (HEYMSFIELD *et al.* 1998, 2010).

The goal of this study was to describe a three-dimensional, mesoscale numerical modeling approach to simulate the microphysical characteristics of ice fog and present the preliminary results as an initial step toward the operational prediction of ice fog. We adjusted the microphysical process in the selected Weather Research and Forecasting (WRF) model version 3.2 (SKAMAROCK *et al.* 2008) using observational data. The effects of the various water vapor emission sources on the formation of ice fog were investigated with the modified modeling capabilities. The following section describes the main observed characteristics during several ice fog events in Interior Alaska. A detailed explanation of relevant modification of the ice microphysical processes in WRF is given in Sect. 3. Section 4 introduces the numerical experimental design and the results from the numerical simulation are followed in Sect. 5. Discussions and a summary of this work follow, in Sects. 6 and 7, respectively.

2. *Observations*

Ice fog has been monitored in Interior Alaska at various locations in Fairbanks and at the nearby Eielson Air Force Base during the winter months of January and February 2012. Three severe ice fog events occurred from 27–31 January 2012. The NCAR Video Ice Particle Sampler (VIPS) and microscope slides with formvar (polyvinyl formal) were deployed to derive ice fog crystal microphysics.

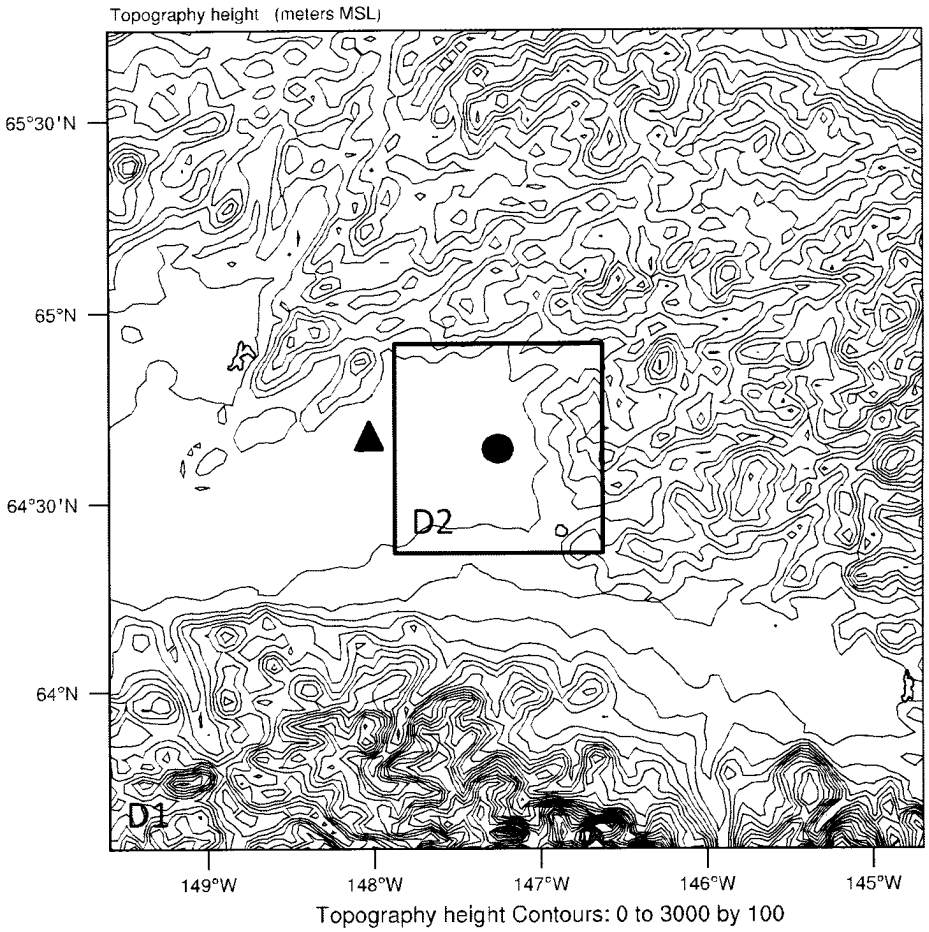

Figure 1
The WRF domain setting with elevation *contour lines* in meters (a.s.l.). The *closed circle* and *triangle* indicate the location of the Eielson Air Force Base (HPP) and the Fairbanks International Airport, respectively

SCHMITT *et al.* (2013) describes the observational methods and the detailed ice fog particle analysis used for this study.

2.1. Synoptic Conditions

Ice fog occurrence was observed from the January 28, 2012, 06 UTC (21:00 local standard time, LST) until 06 UTC of the January 31, 2012 near the Eielson Air Force Base (64.67°N, 147.09°W), southeast from Fairbanks (Fig. 1). The meteorological instruments at the Eielson Air Force Base measure visibility, T, and mean sea level pressure (MSLP) every hour. The synoptic weather situation for January 25–28, 2012, is shown in Fig. 2. At 00 UTC of January 25, 2012, the center of a low pressure zone was located over the south of Alaska (Fig. 2a). As the migratory anticyclone moves to the interior of Alaska, the intensity of low pressure weakens (Fig. 2b, c). Six hours before the onset of the ice fog (00 UTC January 28, 2012), the anticyclonic flow dominates the synoptic situation (Fig. 2d). This weather situation is similar to the conditions described in BOWLING *et al.* (1968) that lead to a high frequency of occurrence of ice fog in Fairbanks: when migratory high pressure moves from Siberia across Alaska.

Figure 3 shows the vertical profiles of equivalent potential temperature (θ_e) derived from the Fairbanks International Airport 00 UTC radiosonde launches during the period 27–30 January 2012. The sounding of January 27, 2012, showed that there was no surface inversion before the migratory anticyclone dominated central Alaska. A surface inversion with a temperature lapse rate of 10.9 °C $(100\ \text{m})^{-1}$ was observed

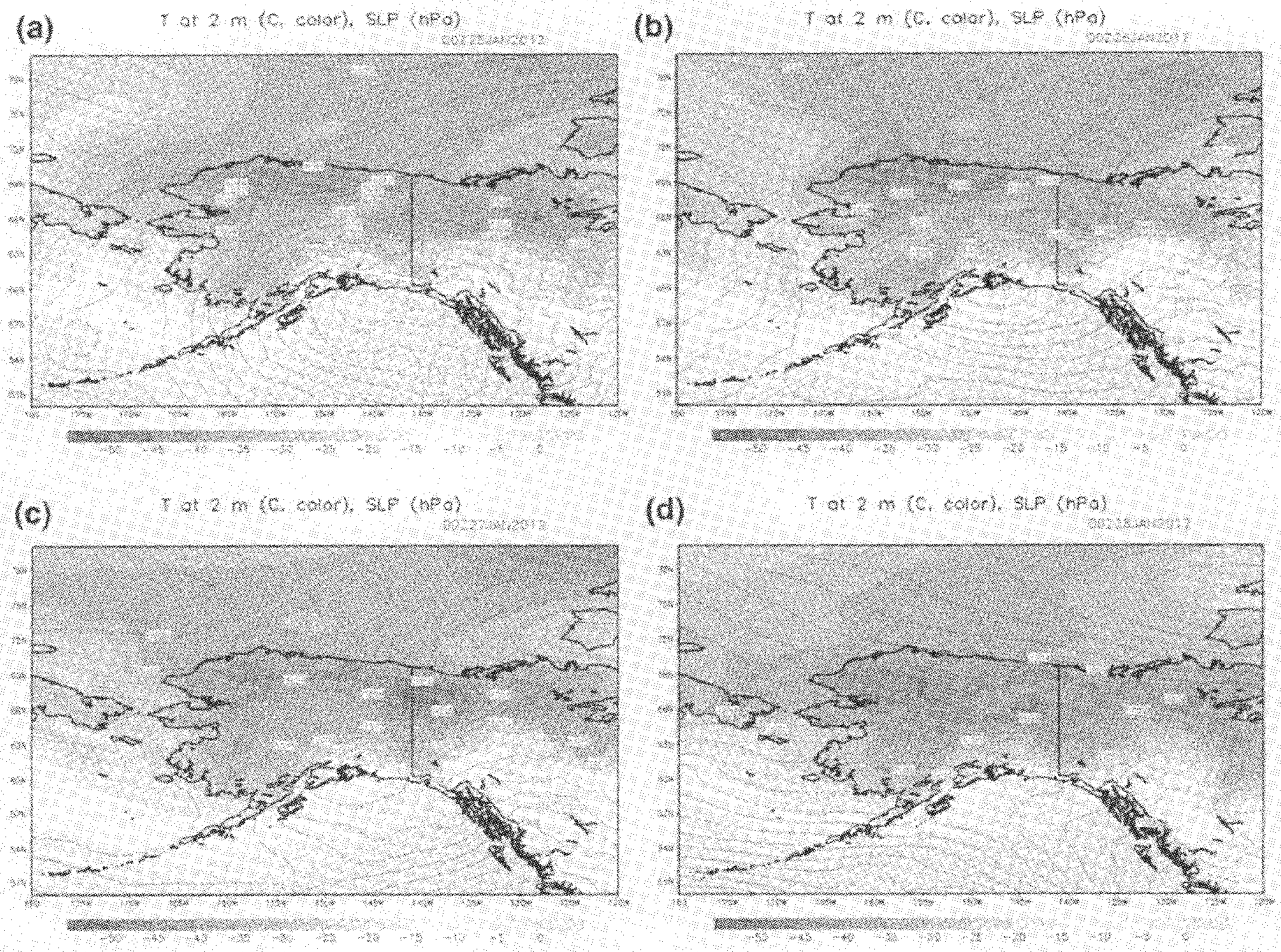

Figure 2
Surface weather map at 00 UTC 25 (**a**), 26 (**b**), 27 (**c**) and 28 (**d**) January 2012. The *contour lines* indicate the mean sea level pressure (hPa), *shaded* areas denote the air temperature at a 2-m altitude (°C). The surface weather map is built from output from NARR

6 h before the onset of ice fog (00 UTC January 28, 2012). During the ice fog event (00 UTC 29–30 January 2012), the surface inversion persisted with a slightly weaker intensity (4.2–6.0 °C (100 m)$^{-1}$). Welch *et al.* (1986), and Kim and Yum (2012) have demonstrated through the numerical modeling that the outgoing longwave radiation at the fog top can induce convective motion within the fog layer, and consequently, the fog top height is lifted. However, it is not clear if the inversion layer is affected by the longwave radiative forcing at the fog top, because the radiosonde site at the Fairbanks International Airport is 48 km away from the Eielson Air Force Base. A time series of T at a 2-m altitude, visibility, and mean sea level pressure (MSLP) is given in Fig. 4. The T gradually decreases with some fluctuations as the migratory anticyclone approaches to Fairbanks. The

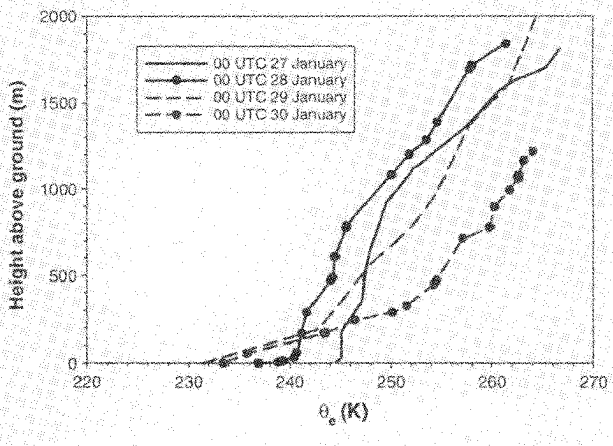

Figure 3
Vertical profiles of equivalent potential temperature (θ_e, K) at 00 UTC 27 (*solid line*), 28 (*solid line* with *closed circle*), 29 (*dashed line*) and 30 (*dashed line* with *closed circle*), measured at the Fairbanks International Airport

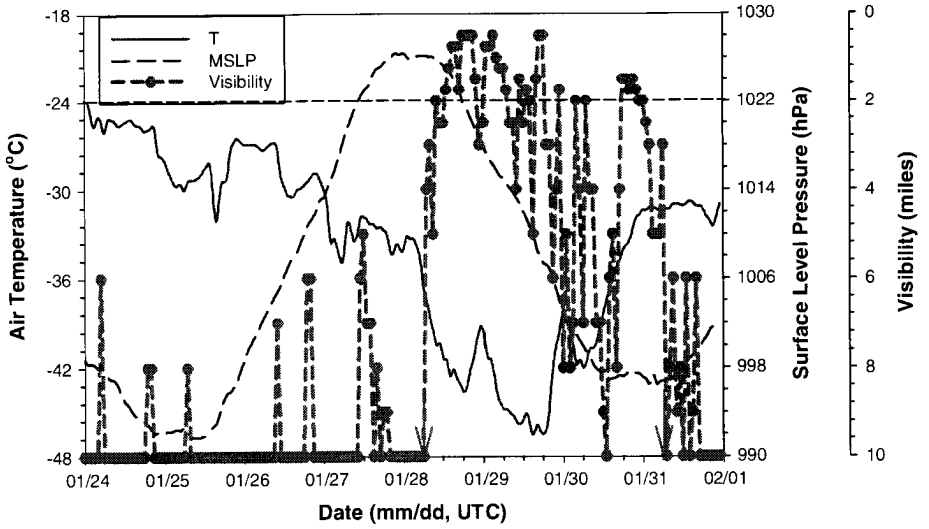

Figure 4
Time series of air temperature at a 2-m altitude (*T*, *solid line*), mean sea level pressure (MSLP, *dashed line*), and visibility (*dotted line*) measured at the Eielson Air Force Base during 24–31 January 2012. The *arrows* indicate the observed onset and dissipation times of ice fog

air still cools to the minimum T of −46.5 °C even as the MSLP decreases (Fig. 4). Then, T increases to −30 °C during the fog dissipation stage.

2.2. *Microphysical Characteristics*

The measurements of ice fog particles were carried out at various environmental conditions. The detailed characteristics of ice fog microphysics are explained in SCHMITT *et al.* (2013). A brief overview of our observations are shown herein. Figure 5 gives the time series of observed ice number concentrations (N_i) and derived ice water content (IWC), measured at the Eielson Air Force Base from 01 UTC to 15 UTC of January 29, 2012. The mean N_i is 26.5 cm^{-3}, which is lower than N_i derived from the study by KUMAI (1966). Additional observations by OHTAKE and HUFFMAN (1969) showed that mean N_i ranges from 30 to 668 cm^{-3} for eight ice fog cases. In our observations, the standard deviation and maximum value of N_i are 31.0 and 99.4 cm^{-3}, respectively, and the formation characteristics of ice fog particles are sensitive to the local meteorological situation such as water vapor variability. The derived IWC shows a larger fluctuation than N_i with a mean IWC of 0.012 g m^{-3} (Fig. 5b). Although the IWC is similar between the two times, 03 and 06 UTC of January 29, 2012, N_i at 03 UTC is about three times higher than at 06 UTC (96.9 vs. 34.1 cm^{-3}). This contrary behavior is due to the difference of size particle distributions between the two times. Figure 6 shows the respective size distributions of the ice fog particles. The N_i for particles larger than 25 μm are 0.48, and 3.4 cm^{-3} at 03 UTC and 06 UTC of January 29, respectively (Fig. 6a, b). The high N_i for larger size contributes to the increase of IWC. The size distribution of ice fog particles is a crucial factor affecting the IWC variability. For the ice habit, the ice fog particles larger than 10 μm are mostly hexagonal plates, and the ice fog particles smaller than 10 μm are typically a mixture of plates and quasi-spherical ice, including the faceted droxtals (SCHMITT *et al.* 2013). Within a former study, KUMAI (1966) reported the number of ice fog particles with spherical shapes with 99 out of 105 cm^{-3} collected during an ice fog case at −42 °C.

3. *Modification of Ice Microphysics Process*

We use the WRF model version 3.2 to evaluate the performance for ice fog particle nucleation. The Thompson scheme (THOMPSON *et al.* 2004, 2008) is used to describe the cloud microphysics in our simulation. The Thompson scheme includes five hydrometeor classes (cloud water, rain, ice crystal, snow, and graupel); water vapor and the number

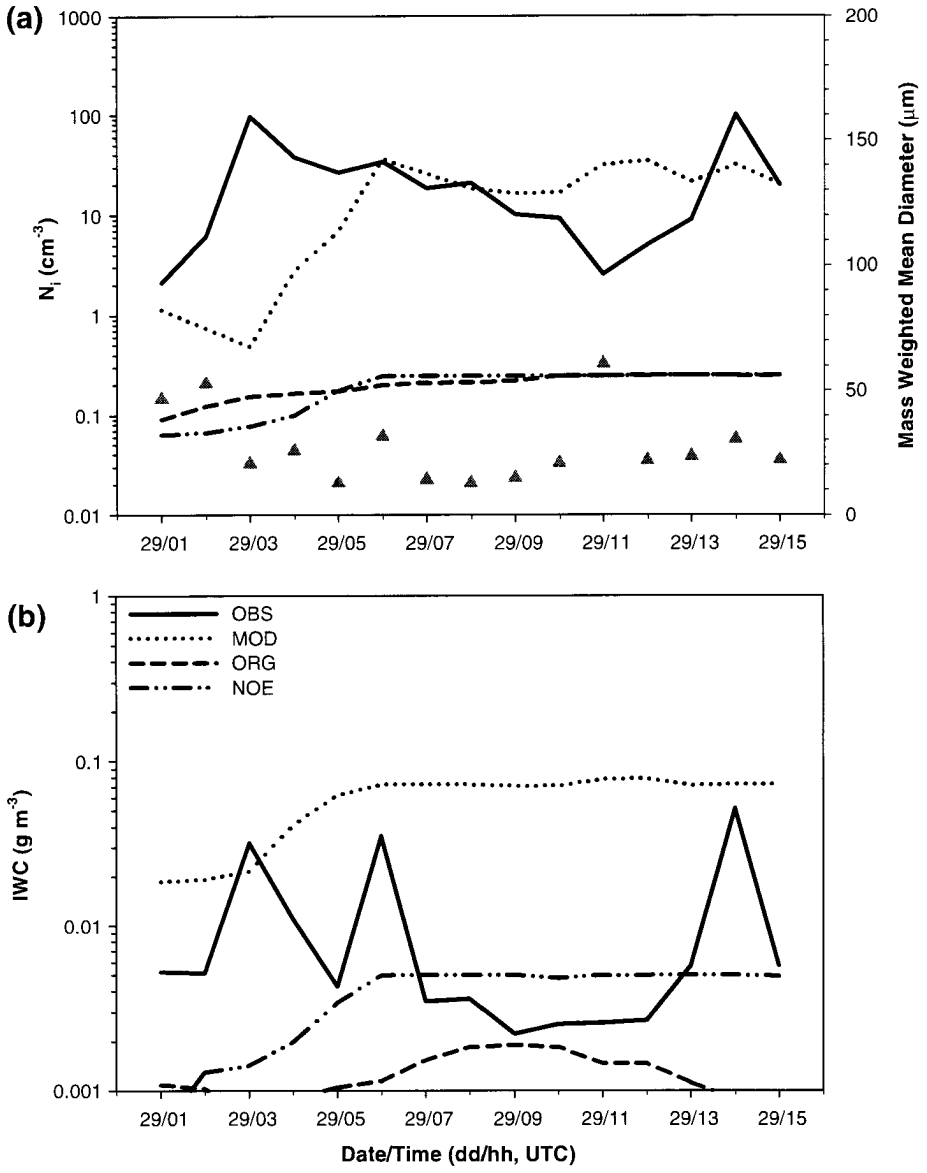

Figure 5
Time series of the number concentration (N_i) and mass-weighted mean diameter (MWMD, *triangle*) of ice fog particles (**a**) and ice water content (IWC) (**b**). The *solid*, *dotted*, *dashed*, and *dash-dot lines* indicate the observation (OBS), the MOD, ORG, and NOE experiments, respectively

concentration of ice crystals and rain are treated as prognostic variables. Microphysical processes for ice crystals include ice crystal formation from primary heterogeneous nucleation and secondary ice multiplication, depositional growth, accretion, riming, and aggregation. The first two processes are related to the production of ice crystals. Depositional growth calculates the increase or decrease in the mixing ratio of ice crystals, based on the ambient concentration of water vapor. The last three processes contribute to the decrease in the mixing ratio and number concentration of ice crystals to generate snow and graupel. However, homogeneous freezing is implicitly taken into account as a part of the heterogeneous freezing process, even though the homogeneous freezing process has a significant impact on cirrus clouds as well as ice fogs (KÄRCHER and LOHMANN 2002; LIU *et al.* 2007). As mentioned in Sect. 2.1, there is no supercooled liquid water in the cloud at extremely low T around −40 °C (CURRY *et al.* 1990). Therefore,

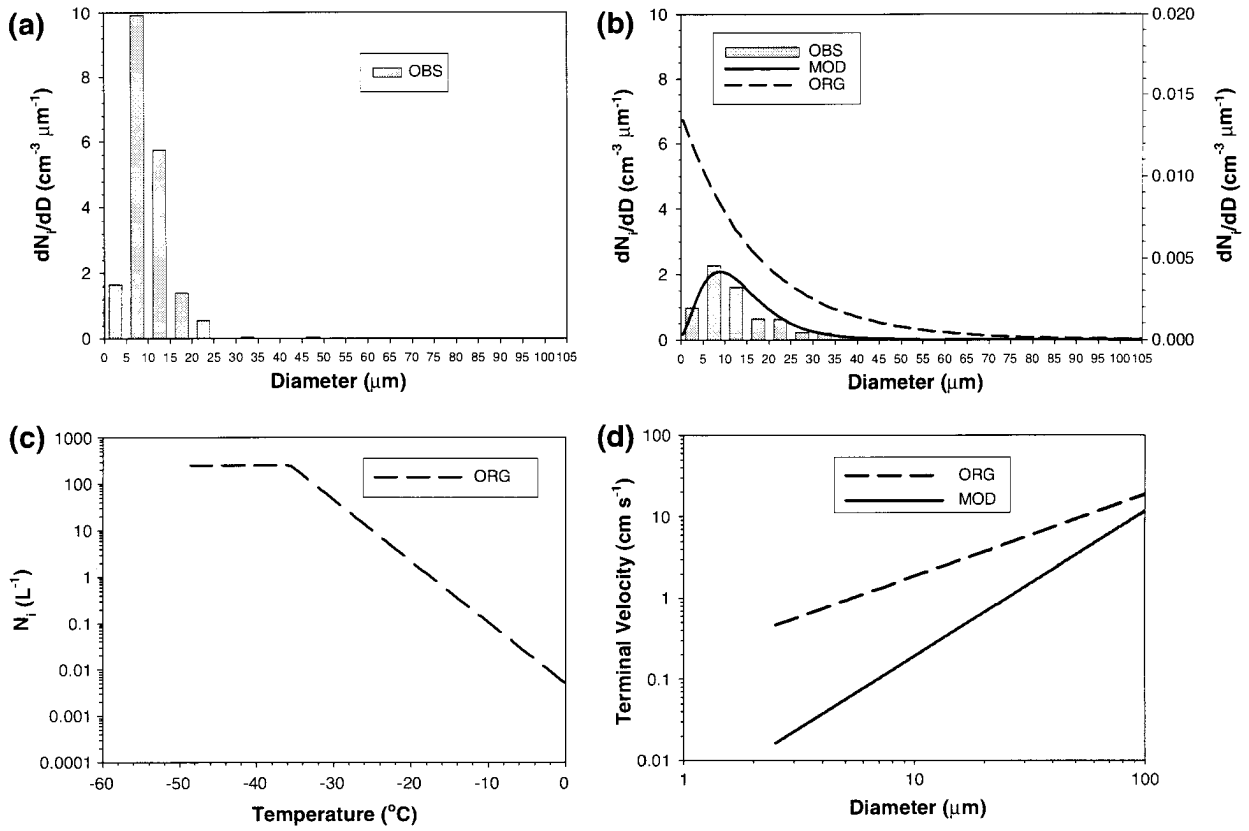

Figure 6
The size distribution of ice crystals observed at 03 UTC (**a**) and 06 UTC (**b**) 29 January 2012. The simulated size distributions of ice crystals from the MOD and ORG experiment are illustrated in (**b**). The number concentration of ice crystals (N_i) as a function of T and terminal velocity as a function of diameter from the MOD and ORG experiment are given in (**c**) and (**d**), respectively. Terminal velocity of MOD is employed from the measurement by SCHMITT *et al.* (2013). In each plot, the *solid and dashed lines* indicate the MOD and ORG experiments, respectively

the present study focuses on the implementation of the homogeneous freezing process and a modification of depositional growth.

3.1. Ice Nucleation

ROGERS and YAU (1989) suggested the schematic picture of four heterogeneous nucleation processes. Ice crystals are produced in the Thompson scheme via deposition and condensation freezing when supersaturation with respect to ice is attained. This is parameterized as a function of T, based on the observation by COOPER *et al* (1986). Figure 6c represents the relationship between the number concentration N_i and T, employed in the original Thompson scheme. N_i due to the deposition and condensation freezing exponentially increases as T decreases. The number concentration N_i reaches its maximum at a selected T threshold of -36 °C and is held constant for temperatures colder than -36 °C.

Recently, most of the mesoscale numerical models employ an explicit parameterization for the contact and immersion nucleation processes. WALKO *et al.* (1995) implemented the contact nucleation process into the regional atmospheric modeling system (RAMS), based on the study of YOUNG (1974). The original Thompson scheme employs the probability function of BIGG (1953) to consider the production of ice crystals via contact and immersion nucleation processes. Nevertheless, four heterogeneous nucleation processes cannot explain the observed mean concentration N_i, 26.5 cm^{-3} (note the unit), as mentioned in Sect. 2.2. Therefore, this study attempted to explicitly calculate the homogeneous freezing of inactivated haze droplets, as well as supercooled liquid water to include the influence of

haze droplets on the production of ice fog particles at high RH and low T. Here, we introduce the homogeneous nucleation processes, which are implemented into the original Thompson scheme.

3.1.1 A. Homogeneous Freezing of Supercooled Liquid Water

This study used the parameterization from the study by DeMott *et al.* (1994), who made an effort to improve the homogeneous freezing processes in the mesoscale model with bulk microphysics. They distinguished between cloud water and inactivated haze droplets as separate populations. A detailed explanation is given in DeMott *et al.* (1994). The number concentration of cloud droplets freezing in time step Δt, $N_{f,s}$, may be formulated as follows:

$$N_{f,s} = \int_0^\infty (1 - exp(-J_s V_l \Delta t) n(D) dD, \qquad (1)$$

where J_s is nucleation rate of pure water, V_l is the volume of droplets, and $n(D)$ is the size distribution of cloud droplets. The rate, J_s, is approximated as a function of T as

$$J_s = 10^y, \qquad (2)$$

with $y = -606.3952 - (52.6611T) - (1.7439T^2) - (0.0265T^3) - (1.536 \times 10^{-4}T^4)$ (Heymsfield and Milosevich 1993). As illustrated in Fig. 7a, this function is also in good agreement with DeMott and Rogers (1990) and Sassen and Dodd (1989) between -30 and -50 °C. The total number concentration of cloud droplets, N_c, is required to get the $N_{f,s}$ in the integral from of Eq. (1). N_c is prescribed as 100 cm^{-3} in the original Thompson scheme. For the calculation of V_l, we use the mean volume diameter of cloud droplets in accordance with Milbrandt and Yau (2005). This study set a thresholds value for the activation of homogeneous freezing of supercooled liquid water as -35 °C.

3.1.2 B. Homogeneous Freezing of Haze Droplet

In many cases, ice crystals in cirrus clouds may form below -38 °C and below water saturation where freezing can occur on solution droplets or haze droplets (Sassen and Dodd 1989). Chen *et al.* (2000) studied the ice formation on the ammoniated sulfate and sulfuric acid aerosol particles under upper-tropospheric conditions using a continuous flow thermal diffusion chamber, and concluded that wet $(NH_4)_2SO_4$ particles can nucleate ice crystals only at a higher RH with respect to water than deliquescence between -40 and -60 °C. Chelf and Martin (2001) determined the homogeneous nucleation rate of haze droplets, J_h, with a solute mole fraction. The observational study by Cziczo *et al.* (2004) showed that sea salt was often incorporated into cirrus, consistent with homogeneous ice formation by aerosol particles from the marine boundary layer. For these reasons, several investigators attempted to parameterize the homogeneous nucleation of haze droplets of cirrus clouds in mesoscale models (e.g., DeMott *et al.* 1994; Lohmann and Kärcher 2002; Liu *et al.* 2007). DeMott *et al.* (1994) found an approximation for the fractions of haze droplets freezing for a given diameter and water saturation ratio, and then integrated over the haze size spectrum assuming an exponential increase. Lohmann and Kärcher (2002) and Liu *et al.* (2007) determined the newly formed ice crystals via the homogeneous freezing of haze droplets as the formulation in terms of critical supersaturation and updraft.

Meanwhile, Koop *et al.* (2000) concluded that homogeneous freezing is independent of the chemical nature of the solution, but only depends on the water activity of the solution droplets. The water activity of soluble aerosols in the atmosphere, in turn, is largely controlled by the relative humidity. This study follows the findings of Koop *et al.* (2000) for the parameterization of homogeneous freezing of haze droplets. They found the homogeneous nucleation rate of a haze droplet, J_h, as a function of water activity according to Eq. (3),

$$\log(J_h) = -906.7 + 8502\Delta a_w - 26924(\Delta a_w)^2 + 29180(\Delta a_w)^3, \qquad (3)$$

with Δa_w, the difference of water activity between liquid and ice. The water activity of a solution in liquid is defined by

$$a_{w,liq} = \exp\left(-\frac{\upsilon \Phi_s M_w M}{1{,}000}\right), \qquad (4)$$

where υ is a dissociation constant for a solute, Φ_s is the molal osmotic coefficient, M_w is the molecular

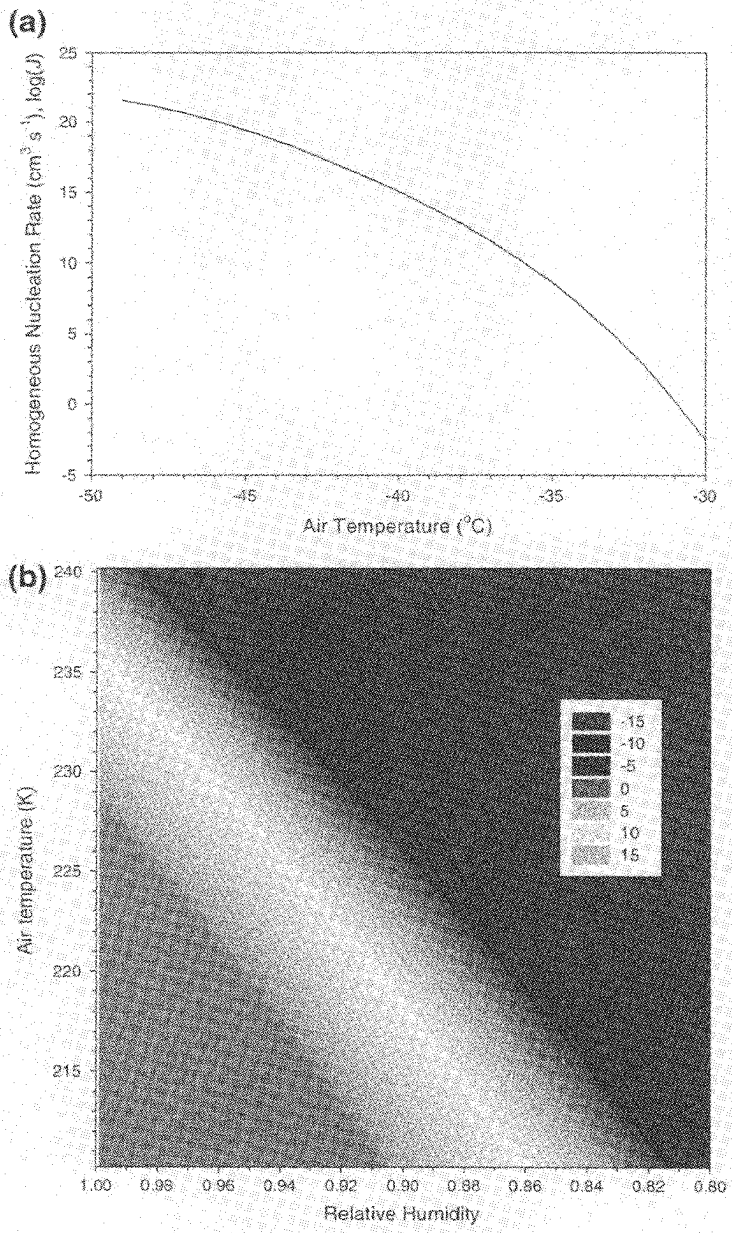

Figure 7
Homogeneous freezing rate of supercooled liquid water ($\log(J_s)$) (**a**) with T and haze droplets ($\log(J_h)$) (**b**) with T and RH. The rates are given in common logarithm

weight of pure water, and M is the molality of the solution. The values for $\upsilon\Phi_s$ were originally obtained by LOW (1969) and then corrected by KUNKEL (1969). This study uses KUNKEL's (1969) values. KOOP *et al.* (2000) formulated the water activity of solution in ice as a function of the temperature T. The radius of a haze droplet, r_h, is given by solving the Köhler equation at a given RH in the present study, and then M is obtained with the assumption that the mass of the solute, ammonium sulfate, is 10^{-12} g. The number concentration of haze droplets freezing, $N_{f,h}$, in time step Δt is calculated in a similar manner to Eq. (1), replacing J_s and V_l with J_h and V_h, respectively. V_h is the volume of a haze droplet with r_h. Because the rate, J_h is only a function of water activity, the total number concentration of haze droplets, N_h, is required to quantify the $N_{f,h}$. We use for the number concentration N_h a value of 300 cm^{-3},

which results from the log-normal distribution during Arctic haze described by the study of SHAW (1983). Figure 7b illustrates the dependence of the rate J_h from RH and T. Our ice fog observations occurred between 225 and 243 K; haze droplets freeze at these temperatures homogeneously at a relative humidity higher than 94 %, in consistence with the results from the laboratory experiment carried out by CHEN *et al* (2000). Activation conditions for homogeneous freezing of haze droplets are T lower than −35 °C and RH is between 82 and 99 % within our presented parameterization scheme.

3.2. Dependence of Ice Crystal Density on Size

The mass and density for individual ice crystals are dependent on the size distribution and typical parameterized values for the density range from 0.91 to 0.1 g cm^{-3} based on the size distribution of ice crystals (HEYMSFIELD *et al.* 2004). Measurements by SCHMITT *et al.* (2013) found that the density of ice fog particles is significantly lower and dependent on particle size, and then presented the ice density, ρ_i (kg m^{-3}) as a function of the diameter D (m) as follows:

$$\rho_i = a_{r\_i} \times D^{b_{r\_i}}, \tag{5}$$

where a_{r_i} and b_{r_i} are 7.22 kg m^{-3} and −0.35, respectively. The present study uses the size-dependent density according to Eq. (5) instead of a constant ice density (typically 890 kg m^{-3}). The following section describes how we calculate the ice water content IWC from the ice density.

3.3. Size Distribution of Ice Crystals

The explicit calculation of the ice water content IWC is more complicated in the double-moment microphysics scheme since it is connected to the size distribution of ice fog particles as well as the ice density. The original Thompson scheme assumes that the ice crystals have the Marshall-Palmer distribution with a mean weighted mass diameter (MWMD) ranging between 20 and 300 μm. In our observations, however, the ice fog particles were distributed according to a Gamma distribution between 1 and 60 μm with a peak at 7.5 μm (Fig. 6b). Consequently, we changed the size distribution of ice crystals according to our observational data from the Marshall-Palmer distribution into the Gamma distribution with the shape factor, $\mu = 2.0$, which is the average value observed during the ice fog episodes as illustrated in Fig. 8. The relationship between IWC, N_i, and ρ_i is given with the Gamma distribution by

$$\begin{aligned} \mathrm{IWC} &= \int \frac{\pi}{6}\rho_i(D)D^3 n(D)\mathrm{d}D \\ &= \int \frac{\pi}{6}a_{r\_i}D^{b_{r\_i}}D^3 \frac{N_i}{\Gamma(\mu+1)}\lambda^{\mu+1}D^{\mu}exp(-\lambda D)\mathrm{d}D \\ &= \frac{\pi}{6}a_{r\_i}\left(\frac{1}{\lambda}\right)^{b_{r\_i}+3} N_i \frac{\Gamma(b_{r\_i}+\mu+4)}{\Gamma(\mu+1)} \end{aligned} \tag{6}$$

where the scale factor, λ, in the model is adjusted by the constraint for the mass-weighted mean diameter (MWMD). Figure 5a shows the MWMD derived from our observational data to be between 13 and 60 μm. Based upon these observations, we adjusted the MWMD to a narrow range from 1 to 125 μm. Finally, the initial mass of ice crystals should be fixed. This study prescribes the initial mass of ice crystals as 4.7 × 10^{-16} kg, which is equivalent to the mass of the sphere with the diameter of 1 μm and the density of 910 kg m^{-3}, as derived from Eq. (5).

3.4. Gravitational Settling

The gravitational settling is a very specific characteristic for each ice fog particle. Ice fog particles are considered as the suspended particles in analogy to fog droplets. In general, the terminal velocity of a particle is expressed by the power law as a function of diameter (STRAKA 2009). The Thompson scheme employs the power law as the terminal velocity from the study of SCHOENBERG FERRIER (1994); a comparison of the originally predicted terminal velocities with the velocities derived from our observational data is shown in Fig. 6d. The terminal velocities calculated from observed particle properties from the study of SCHMITT *et al.* (2013) are significantly slower, especially for ice crystals smaller than 10 μm in diameter. These slow terminal velocities lead to a longer suspension time; we replaced the terminal velocity for the gravitational settling with the Eq. (7) presented in SCHMITT *et al.* (2013).

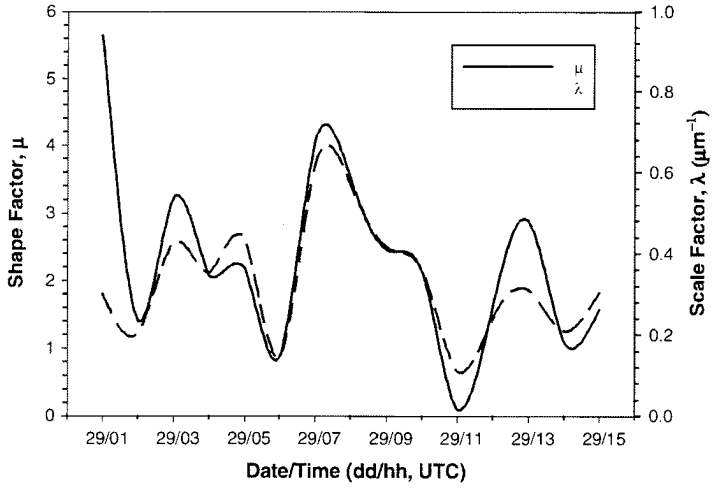

Figure 8
Shape factor, μ and scale factor, λ, for the Gamma distribution used to fit ice fog particle size distribution from the observation

$$v_t(D) = \alpha \times D^{\beta}, \quad (7)$$

where $\alpha = 0.647 \times 10^6$ m s^{-1}, $\beta = 1.73$, D is the diameter (m) for an individual ice crystal, and v_t is terminal velocity (m s^{-1}).

Thus, the present study modifies the ice microphysical processes for the successful simulation of ice fog case. The modifications are summarized as follows:

1. Homogeneous freezing of supercooled liquid water and haze droplets is explicitly calculated.
2. The ice density is treated as a size-dependent variable.
3. The initial mass of newly nucleated ice crystals is changed.
4. The size distribution was changed to a gamma distribution from the previously used Marshall-Palmer distribution.
5. MWMD was changed to be between 1 and 125 μm in diameter for ice crystals.
6. The terminal velocity was reduced for ice crystals to be suspended significantly longer in the air.

4. Numerical Modeling

4.1. Inclusion of Water Vapor Emissions

We added water vapor emissions from the Eielson Air Force Base Heat and Power Plant (HPP) (64.67°N, 147.09°W, Fig. 1) in order to simulate our ice fog observations and to study the influence of anthropogenic water vapor emissions on the formation of ice fog. The emission rates of water vapor from the HPP were previously estimated to be 30 ton h^{-1} (HANKS and HOLDMANN 2009). Water vapor, emitted from the HPP, is dispersed by the wind field, diffused by turbulence, and is transformed to ice crystals due to the nucleation process. Figure 9 presents the flow chart to generate the ice crystals with the dispersion of emitted water vapor from the local sources. The water vapor mixing ratio emitted from the source, q_{ve}, is added into the ambient water vapor mixing ratio, q_v. This study sets the same activation condition by the supersaturation as the original Thompson scheme, i.e., ice crystals are generated via deposition and condensation freezing when the water vapor mixing ratio exceeds 25 % supersaturation with respect to ice. The total water vapor mixing ratio ($q_v + q_{ve}$) enables the ice crystals to be generated when the activation condition is met.

4.2. Numerical Experiment Setup

Figure 1 shows the domain setting for the WRF simulation, where a one-way grid nesting procedure is employed for two domains. Grid spacing of the outer and inner domains is 2.5 km and 500 m, respectively, and the center of the domain is the location of the HPP at the Eielson Air Force Base. The entire grid system has 100 x 100 grid cells and 65 vertical layers with the top level at 100 hPa. The

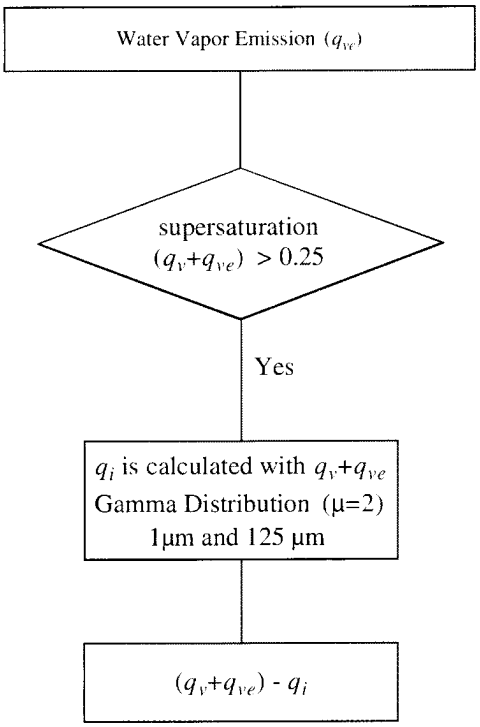

Figure 9
Flow chart for the ice formation process with the emission of water vapor. q_{ve} and q_v are anthropogenic emitted and ambient water vapor, respectively. q_i is ice water content produced by the homogeneous and heterogeneous nucleation processes

moderate resolution imaging spectroradiometer (MODIS) land-cover classification is selected for the land-use categories, and then 'Evergreen Needleleaf Forest' is changed into 'Snow and Ice' since the domain area is permanently covered with snow in winter. The three-hourly data from the North American Regional Reanalysis (NARR), produced by the National Center for Environment Prediction (NCEP), are used as the initial and boundary meteorological conditions for the WRF simulations.

The WRF model configuration is summarized in detail in Table 1. There are three experiments to attain the primary goal of the present study. The set of selected physical parameterization is Rapid Radiative Transfer Model for GCM application (RRTMG) for radiation (SKAMAROCK *et al.* 2008) and Yonsei-University (YSU) for the planetary boundary layer (HONG *et al.* 2006). The experiments of 'MOD' and 'ORG' indicate the numerical simulation with the modified ice microphysics, introduced in Sect. 3, and with the original Thompson scheme, respectively. In

Table 1
Numerical experiment design

	ORG		MOD		NOE	
Grid spacing (m)	D1	D2	D1	D2	D1	D2
	2,500	500	2,500	500	2,500	500
IC/BC	NARR		NARR		NARR	
PBL	YSU		YSU		YSU	
Shortwave radiation	RRTMG		RRTMG		RRTMG	
Longwave radiation	RRTMG		RRTMG		RRTMG	
Microphysics	Original		Modified		Modified	
Water vapor emission	HPP		HPP		–	

order to evaluate the effects of water vapor emissions as an anthropogenic source, the experiment of 'NOE' is performed without the emission. The 36-h simulations in each experiment are executed from 06 UTC of January 28 until 18 UTC of January 29, 2012, and water vapor emission starts 12 h after simulation began in the MOD run. The results in the following sections come from the modeling output for the inner domain.

5. *Results*

5.1. *Modification of Ice Microphysics*

Figure 5 shows the time series of N_i and IWC at the lowest level at the Eielson Air Force Base. The N_i in the MOD experiment is increased remarkably to the values from the observation, even if there are occasionally large differences (i.e., 03 UTC and 11 UTC 29 January), comparing to N_i simulated in ORG experiment. We address these low N_i values to the absence of the homogeneous freezing parameterization in the ORG experiment; supercooled liquid water or haze droplets freeze homogeneously in the MOD experiment. In contrast to the number concentrations, the simulated IWC does not coincide well with IWC derived from our observations. The observed IWC from 07 UTC to 13 UTC January 29, 2012, was reduced to 0.0027 g m^{-3}, though the observed N_i still is higher than 1 cm^{-3} in observation. The decreasing span of IWC will be discussed in the Sect. 6. Comparing the IWC between the ORG and NOE experiments reveal three-times higher IWC values in the NOE experiment despite very similar number

concentrations N_i, as shown in Fig. 5a. The change of the size spectrum into the Gamma distribution makes the characteristic diameter shifted into the larger size, and therefore, higher IWC is obtained by the population for the larger size in the NOE experiment.

Of the modifications in this present study, most noticeable is the size distribution of ice crystals to be changed into the Gamma distribution with MWMD between 1 and 125 μm. Figure 6b shows an example of the size distributions of the ice crystals from the experiment MOD and ORG. Note that the right axis is only used for the ORG experiment. Total N_i values are 34.1, 35.8, and 0.199 cm^{-3} for the OBS, the MOD, and ORG experiments, respectively. The particle size distribution for a 1.0-μm bandwidth in the MOD experiment is given by the Gamma distribution with the assumption of a shape factor, $\mu = 2.0$, and a scale factor, $\lambda = 0.33$ μm^{-1}, which is corresponding to the characteristic diameter, 3.0 μm. The peak value in the MOD experiment is at 8.5 μm, which is almost consistent with the diameter at the peak in the OBS experiment. The number concentration of ice crystals, which have diameters larger than 15 μm, is higher in the MOD than that in the OBS experiment, implying that the size distribution in the model is not perfectly matched with the Gamma distribution. Meanwhile, as expected, the Marshall-Palmer distribution is given in the ORG experiment. Even if the total N_i is largely different between the OBS, the MOD, and ORG experiment, the comparison of the relative frequency in each distribution is meaningful. For the ice crystals larger than 15 μm, the relative frequencies are 28.7, 36.0, and 42.1 % for the OBS, MOD, and ORG experiments, respectively, indicating that the prescribed distributions for MOD and ORG experiments overestimate N_i for the larger ice crystals. Nevertheless, the Gamma distribution is more suitable for the simulation of the ice fog episode because most ice fog particles typically are smaller than 15 μm.

5.2. *Sensitivity Tests*

In the introduction, Benson (1970) referred to an ice fog event as air pollution at extremely low temperatures. Emitted water vapor from power plants and from cars would be crucial source for the formation of ice fog particles because the saturation vapor pressure with respect to ice is as low as 12.85 Pa at −40 °C, which is equivalent to the mixing ratio of 0.079 g kg^{-1} at 1,013 hPa. In Sect. 4.1, we mentioned that the emission rate of water vapor is 30 ton h^{-1} at the HPP. With the horizontal resolution, 500 m, the emission flux density is converted to 5.46×10^{-3} g kg^{-1} s^{-1}, assuming an air density of 1.22 kg m^{-3}. From the above theoretical calculation, the time scale is just 15 s for water vapor saturation with respect to ice formation. The present study identifies the effects of water vapor emissions on the ice fog formation with WRF model simulations with and without (NOE experiment) anthropogenic water vapor sources.

Figure 10 clearly shows the differences in IWC resulting from anthropogenic emissions of water vapor. Ice fog at the lowest model level forms near the HPP in the MOD experiment. In the model, water vapor from the HPP instantly nucleates the ice fog particles and the amount of water vapor is reduced below the lowest contour level for a short time. The calm winds create favorable conditions for the ice fog to last nearby the HPP without notable dissipation by advection (see wind barb in Fig. 10). In contrast to the MOD experiment, there are just a few ice fog patches in the NOE experiment, although the saturation vapor pressure is still low. The sensitivity test clearly reveals that ice fog is produced via homogeneous freezing of supercooled liquid water or haze droplets from anthropogenic water vapor emissions. Meanwhile, the fog depth at the Eielson Air Force Base is shallower than 10 m in Fig. 10c due to the existing strong inversion, which restricts the vertical extent of the ice fog layer. In spite of the suppressing effect of the inversion on the vertical development of the fog layer, the strong inversion also plays a role in making the favorable conditions to form ice crystals by capturing the water vapor emitted from the source point in the early stage of ice fog formation. The relationship between ice crystal production and weak turbulence in a strong inversion is more complicated. Zhou and Ferrier (2008) analyzed how the fog droplet formation is connected to the gravitational settling and turbulent intensity in the case of radiation fog. In their study, the

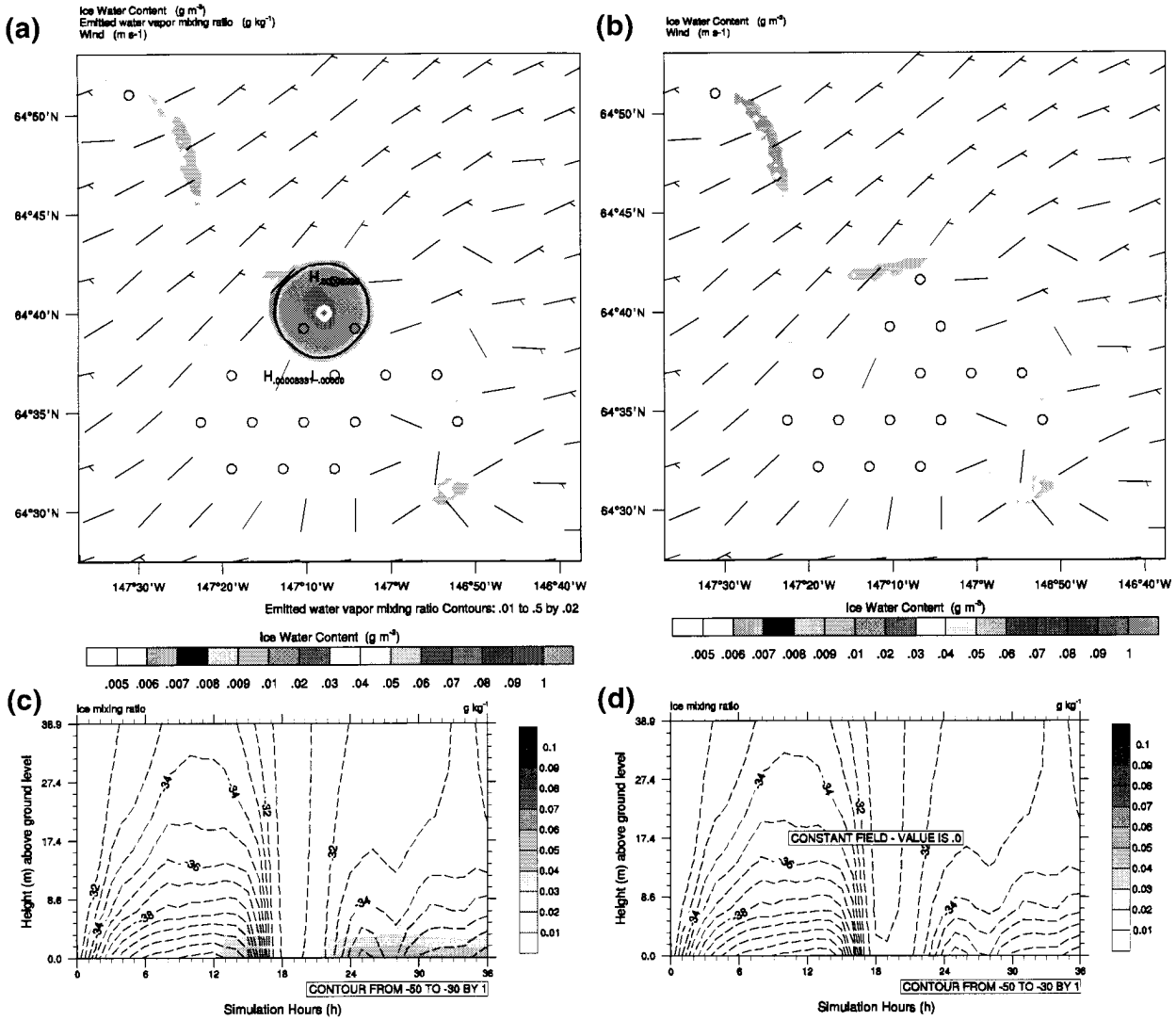

Figure 10
Horizontal distribution at the lowest model level of IWC (*shaded*) and q_{ve} (*contour*) at 21 UTC 28 January 2012 from the MOD (**a**) and NOE (**b**) experiments, and time-height plot of ice-water mixing ratio (*shaded*) and T (*contour*) at the Eielson Air Force Base from the MOD (**c**) and NOE (**d**) runs. *Wind barbs* are given in the plot (**a**) and (**b**)

favorable conditions for the formation of radiation fog are strong cooling and weak turbulence. Water vapor emitted from the source point is captured by the strong inversion in our simulation and ice crystals are likely to be formed in a given condition.

As the inversion strength is weakened, T increases with the reduction of the ice-water mixing ratio from 18 to 21 h after our simulation start-time. It is of interest in comparing T within the ice fog layer in the MOD run, which is slightly higher than that in NOE run. This is due to the latent heat released by the condensation and sublimation of water vapor, which heats the air within the fog layer. Figure 11a also accounts for the effect of the latent heat on the variation of T: the formation of ice crystals from 06 UTC of January 29 leads to the increase of T in the MOD run, whereas T in our ORG experiment is still lower than in the MOD experiment. The microphysical process indicates a clear feedback and is responsible for the difference in the meteorological condition of the boundary layer.

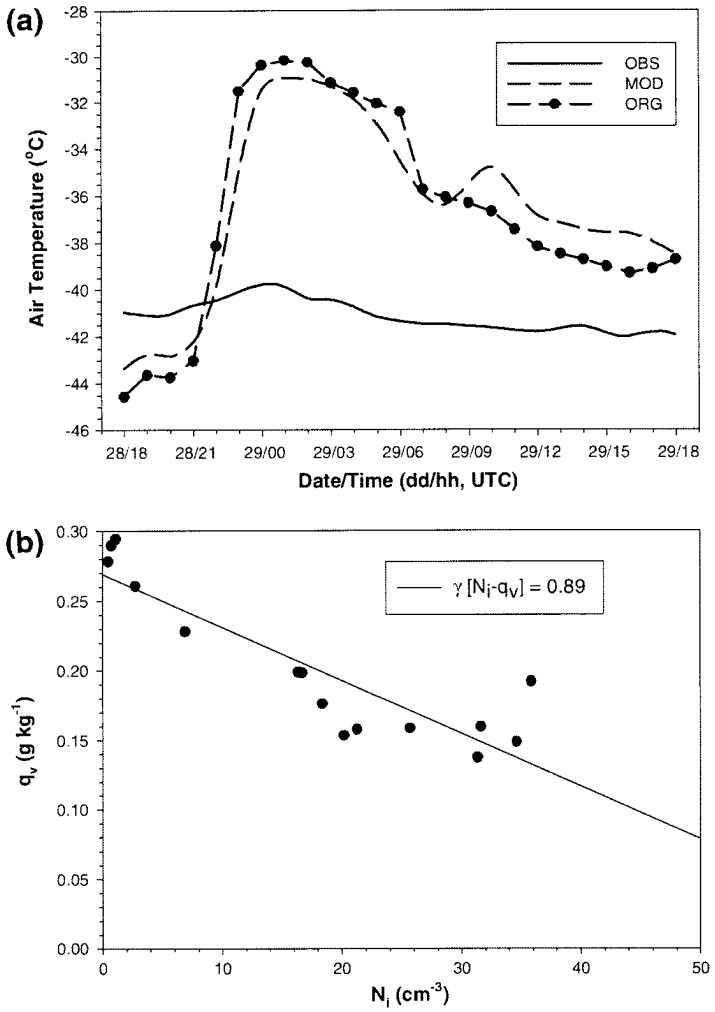

Figure 11
Time series (**a**) of T at a 2-m altitude from the ground surface from the OBS (*solid line*), MOD (*dashed line*), and ORG (*dashed line with closed circle*) experiments, and *scatter plot* (**b**) of N_i and q_v from the MOD

6. Discussion

There are two significant differences of N_i (03 UTC and 11 UTC of January 29) in Fig. 5a: the MOD experiment underestimates N_i at 03 UTC of January 29, whereas ice fog particles at 11 UTC of January 29 are predicted to be higher in concentration in the MOD experiment than the OBS. In Fig. 11a, the modeled temperature T at 2 m altitude at 03 UTC 29 January is overestimated by 9.4 °C in the MOD experiment, when compared to the observed temperature. This warm bias is also found in the ORG run, implying that this is not the direct result from the modification. The relatively higher T in the modeling may be accounted for by the release of latent heat due to the condensation and sublimation of water vapor, and then the latent heat released could be captured in the shallow layer just above ground by the strong inversion. In the both experiments, MOD and ORG, snow was produced by the water vapor diffusion but the snow was not measured at that time, which means that the microphysics should be modified to reduce the snow generation rate due to the sublimation of water vapor. The overestimated growth of ice crystals to snow due to the water vapor diffusion largely causes the latent heat to be released, and therefore, the T at 2 m altitude becomes higher than the observation. This modeled warmer condition does not lead to the production of ice fog particles by homogeneous freezing because the activation condition of

T for homogeneous freezing is not satisfied, i.e., $T > -35$ °C. Besides, warmer air results in high-saturation vapor pressure with respect to ice, which contributes to evaporating ice fog particles. This accounts for a negative correlation between N_i and q_v in Fig. 11b, which means that evaporating ice fog particles leads to the increase of the water-vapor mixing ratio in relatively warm conditions. Therefore, N_i is lower in the MOD experiment than in the observations (OBS). Since 03 UTC of January 29, 2012, the simulated N_i increases rapidly with a sharp reduction of T, as can be seen in Fig. 11a. N_i is kept nearly constantly, satisfying the activation conditions for homogeneous freezing (see Fig. 11a, T is still lower than −35 °C). Contrary to the modeling, the observed N_i decreases gradually, with the largest difference in N_i from the MOD run at 11 UTC of January 29, 2012. The observed mean q_v in the observation is 0.097 g kg^{-1}, much lower than 0.21 g kg^{-1} in the modeling for the period of a decreasing span of N_i. This may be why the modeling overestimates the N_i. Furthermore, a reduction of observed IWC results in the large deviation in IWC between the MOD experiment and OBS during the decreasing span of N_i (Fig. 5b). Equation (6) indicates that the IWC can be sensitive to the shape and scale factors of the Gamma distribution. In the given λ, N_i and ρ_i, for example, IWC is only determined by the shape factor, μ. IWC increases in proportion to the cube of the factor μ (not shown). One can conclude that the extremely low IWC results from the abrupt change of μ, considering that μ largely fluctuates from 4.0 to 0.1 in Fig. 8. The current numerical model with bulk microphysics has the limitation to change the scale and shape factor in each time step, implying that the final goal is to employ the bin microphysics for the successful simulation of ice fog.

There is still no clear evidence as to which nucleation process contributes to the formation of the ice fog particles in a given condition. Kumai (1966) concluded through his measurements using electronic microscope analysis that ice fog particles were generated by the heterogeneous nucleation. Recently, however, several studies on the effects of ammonium sulfate on the formation of ice crystals in cirrus demonstrated that soluble aerosols at a relative humidity (RH) higher than deliquescence may freeze as ice crystals (e.g., Chen *et al.* 2000; Chelf and Martin 2001). Figure 12 shows the time series of ice crystal production rates from deposition, and homogeneous freezing of supercooled liquid water and haze droplets with T and RH from the MOD experiment. Prior to the emission of water vapor, ice fog particles are produced only by the deposition with the rate of 0.15 L^{-1} s^{-1}. As soon as the water vapor is emitted, homogeneous freezing rates increase rapidly at 19 UTC January 28, 2012, consuming water vapor via the diffusion growth of ice fog particles (see Fig. 11b. N_i is negatively correlated to q_v). Haze droplets still freeze due to the relatively low T, even with the RH around 93 %, until 23 UTC January 28, 2012. In contrast, at the relatively higher T than −35 °C, which is the threshold value for activating homogeneous freezing, from 01 to 04 UTC January 29, 2012, homogeneous freezing does not occur; though the RH exceeds 100 %, which is consistent with the lowest N_i in the MOD experiment at 03 UTC of January 29, 2012. One can conclude that the homogenous freezing of haze droplets as well as supercooled liquid water is more sensitive to the T than to RH. Therefore, ice fog particles result from homogeneous freezing at the relatively low T.

7. *Summary and Conclusions*

We described a modification of the Thompson microphysics scheme in WRF version 3.2 to model the formation of ice particles during the observed extreme ice fog cases from 06 UTC 28 January to 31 January 2012. The microphysical characteristics of ice fog are different from those of typical ice clouds, and therefore, the ice microphysics processes, which are developed using the observed data for ice clouds, needed to be modified to simulate the ice fog particles. Observational data was used to implement a homogeneous freezing parameterization, and to improve the particle size distribution and gravitational settling. For the sophisticated ice microphysics, the present study separates between supercooled liquid water and haze droplets for the homogeneous freezing. The homogeneous freezing rate of supercooled liquid water is employed as a function of air temperature to obtain the number concentration of

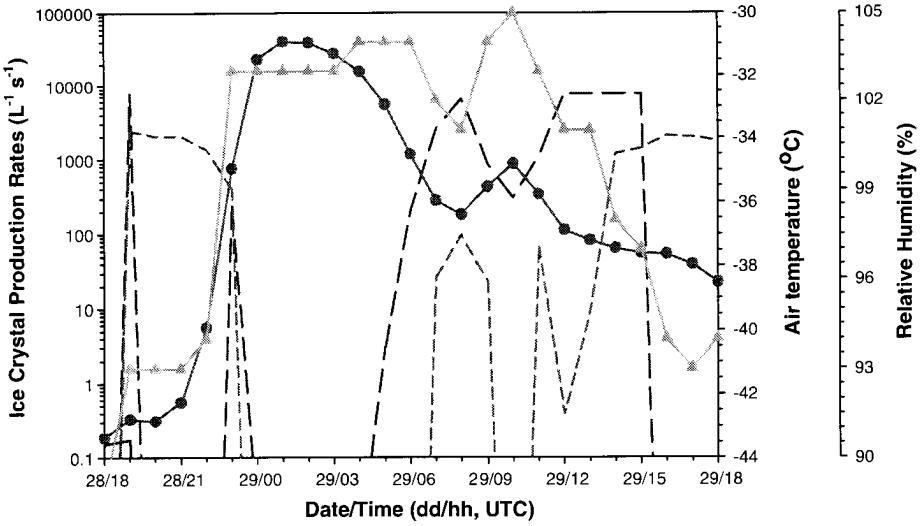

Figure 12
Time series of ice crystal production rate from deposition (*black solid line*), homogeneous freezing of supercooled liquid water (*blue long-dashed line*) and haze droplets (*red short-dashed line*), *T* (*green solid line* with *circle*), and RH (*gray solid line* with *triangle* from the MOD simulation

homogeneously freezing cloud droplets. Moreover, there are various ways to parameterize the homogeneous freezing of haze droplets, but the present study follows the nucleation rate of haze droplets as a function of water activity from the findings of KOOP *et al.* (2000). In agreement with observed ice crystal numbers, the implemented homogeneous freezing processes resulted in a significantly higher N_i than the original Thompson scheme. Our observations showed that the ice particles have a Gamma distribution with the peak at diameters smaller than 10 μm. Furthermore, gravitational settling was adjusted, enabling ice particles to be suspended longer as ice fog precipitates much slower than other types of ice clouds. The slow terminal velocity played a role in increasing the time scale for the ice particles to settle to the ground surface. Sensitivity tests contributed to understanding the effects of water vapor emissions as an anthropogenic source on the formation of ice fog. We can conclude from the NOE experiments that ice fog can be significantly increased by anthropogenic activities.

Note that the herein described microphysics scheme is based upon measurements of ice fog in a subarctic setting. The presented modified Thompson microphysics scheme is not applicable for explicit predictions of other phenomena, such as aircraft icing for example. Our measurements revealed two orders of magnitude higher ice crystal concentrations and significantly slower terminal velocities than what was found in typical natural ice clouds in the upper troposphere and lower stratosphere. Therefore, our modification would result in a significantly higher occurrence of high ice clouds by using the presented microphysics in other geographical areas. However, the high ice crystal concentrations in ice fog are comparable to in situ measurements of ice crystal concentrations found in aircraft condensation trails during the SUbsonic aircraft: Contrail and Cloud Effects Special Study (SUCCESS) program (HEYMSFIELD *et al.* 1998, 2010).

The major findings of the present study are preliminary results from the modeling output, and may be sensitive to the measurement of the microphysical characteristics of ice fog, which means that the microphysics used in this study cannot account for all kinds of clouds, e.g., cirrus clouds. As an initial step to forecasting the ice fog in the Arctic region, we present a modification of microphysics using an explicit calculation of homogeneous nucleation to better understand the nature of ice fog.

Ice fog is deeply correlated to local air pollution, such as that caused by combustion products from cars. Future and more applicable numerical models need to include anthropogenic emissions of water vapor to resolve and better understand phenomena such as ice fog. Additional chemical reactions

affecting ice fog microphysics may be studied with chemical models integrated in numerical meteorological models. As an example of such a model, WRF with online Chemistry (WRF-CHEM, GRELL *et al.* 2005) can provide further insights in the relationship between ice fog and air pollution using the sophisticated ice microphysics improvements from the present study.

Acknowledgments

This work was funded by an award from the U.S. Air Force (Award Number, FA 9550-11-1-0006).

REFERENCES

BENSON, C. S., 1970: ICE FOG. *Weather, 25*, 11–18.

BIGG, E. K., 1953: The formation of atmospheric ice crystals by the freezing of droplets. *Quart. J. Roy. Meteor. Soc., 79*, 510–519.

BIGG, E. K., 1996: Ice forming nuclei in the high Arctic. *Tellus, 48*, 223–233.

BOWLING, S. A., T. OHTAKE, and C. S. BENSON, 1968: Winter Pressure Systems and Ice Fog in Fairbanks, Alaska. *J. Appl. Meteor., 7*, 961–968.

CHELF, J. H. and S. T. MARTIN, 2001: Homogeneous ice nucleation in aqueous ammonium sulfate aerosol particles. *Journal of Geophysical Research: Atmospheres, 106*, 1215–1226.

CHEN, Y., P. J. DEMOTT, S. M. KREIDENWEIS, D. C. ROGERS, and D. E. SHERMAN, 2000: Ice Formation by Sulfate and Sulfuric Acid Aerosol Particles under Upper-Tropospheric Conditions. *J. Atmos. Sci., 57*, 3752–3766.

COOPER, W. A., 1986: Ice Initiation in Natural Clouds. *Meteorological Monographs, 21*, 29–32.

CURRY, J. A., F. G. MEYER, L. F. RADKE, C. A. BROCK, and E. E. EBERT, 1990: Occurrence and characteristics of lower tropospheric ice crystals in the arctic. *Inter. J. Climatology, 10*, 749–764.

CURRY, J. A., and COAUTHORS, 2000: FIRE Arctic Clouds Experiment. *Bull. Amer. Meteor. Soc., 81*, 5–29.

CZICZO, D. J., D. M. MURPHY, P. K. HUDSON, and D. S. THOMSON, 2004: Single particle measurements of the chemical composition of cirrus ice residue during CRYSTAL-FACE. *J. Geophy. Res.: Atmospheres, 109*, doi:10.1029/2003jd004032.

DEMOTT, P. J. and D. C. ROGERS, 1990: Freezing Nucleation Rates of Dilute Solution Droplets Measured between −30° and −40°C in Laboratory Simulations of Natural Clouds. *J. Atmos. Sci., 47*, 1056–1064.

DEMOTT, P. J., M. P. MEYERS, and W. R. COTTON, 1994: Parameterization and Impact of Ice initiation Processes Relevant to Numerical Model Simulations of Cirrus Clouds. *J. Atmos. Sci., 51*, 77–90.

GIRARD, E. and J.-P. BLANCHET, 2001: Microphysical Parameterization of Arctic Diamond Dust, Ice Fog, and Thin Stratus for Climate Models. *J. Atmos. Sci., 58*, 1181–1198.

GIRARD, E. and J.-P. BLANCHET, 2001: Simulation of Arctic Diamond Dust, Ice Fog, and Thin Stratus Using an Explicit Aerosol–Cloud–Radiation Model. *J. Atmos. Sci., 58*, 1199–1221.

GRELL G.A., S.E. PECKHAM, R. SCHMITZ, S.A. MCKEEN, G. FROST, W.C. SKAMAROCK, and B EDER. 2005. Fully coupled 'online' chemistry in the WRF model. *Atmos. Environ., 39*:6957–6976.

GULTEPE, I., T. KUHN, M. PAVOLONIS, C. CALVERT, J. GURKA, A. J. HEYMSFIELD, P. S. K. LIU, B. ZHOU, R. WARE, B. FERRIER, J. MILBRANDT, and B. BERNSTEIN, 2013: ICE FOG IN ARCTIC DURING FRAM-ICE FOG PROJECT: AVIATION AND NOWCASTING APPLICATIONS. *Bull. Amer. Meteor. Soc.* In Print.

HEYMSFIELD, A., D. BAUMGARDNER, P. DEMOTT, P. FORSTER, K. GIERENS, and B. KÄRCHER, 2010: Contrail Microphysics. *Bull. Amer. Meteor. Soc., 91*, 465–472.

HEYMSFIELD, A. J. and L. M. MILOSHEVICH, 1993: Homogeneous Ice Nucleation and Supercooled Liquid Water in Orographic Wave Clouds. *J. Atmos. Sci., 50*, 2335-2353.

HEYMSFIELD, A. J., R. P. LAWSON, and G. W. SACHSE, 1998: Growth of ice crystals in a precipitating contrail. *Geophy. Res. Lett., 25*, 1335–1338.

HONG, S. Y., Y. NOH, and J. DUDHIA, 2006: A new vertical diffusion package with an explicit treatment of entrainment processes. *Mon. Wea. Rev., 134*, 2318–2341.

HUFFMAN, P. J. and T. OHTAKE, 1971: Formation and Growth of Ice Fog Particles at Fairbanks, Alaska. *J. Geophys. Res., 76*, 657–665.

KÄRCHER, B. and U. LOHMANN, 2002: A parameterization of cirrus cloud formation: Homogeneous freezing of supercooled aerosols. *J. Geophys. Res., 107*, AAC 4-1-AAC 4-10.

KIM, C. and S. YUM, 2012: A Numerical Study of Sea-Fog Formation over Cold Sea Surface Using a One-Dimensional Turbulence Model Coupled with the Weather Research and Forecasting Model. *Boundary-Layer Meteor., 143*, 481–505.

KOOP, T., B. LUO, A. TSIAS, and T. PETER, 2000: Water activity as the determinant for homogeneous ice nucleation in aqueous solutions. *Nature, 406*, 611–614.

KUMAI, M., 1966: Electron Microscopic Study of Ice-Fog and Ice-Crystal Nuclei in Alaska. *J. Meteor. Soc. of Japan., 44*, 185–194.

KUNKEL, B. A., 1969: Comments on "A Generalized Equation for the Solution effect in Droplet Growth". *J. Atmos. Sci., 26*, 1344–1344.

KUNKEL, B. A., 1984: Parameterization of Droplet Terminal Velocity and Extinction Coefficient in Fog Models. *J. Appl. Meteor., 23*, 34–41.

LIU, X., J. E. PENNER, S. J. GHAN, and M. WANG, 2007: Inclusion of Ice Microphysics in the NCAR Community Atmospheric Model Version 3 (CAM3). *J. Climate, 20*, 4526–4547.

LOHMANN, U. and B. KÄRCHER, 2002: First interactive simulations of cirrus clouds formed by homogeneous freezing in the ECHAM general circulation model. *J. Geophys. Res., 107*, AAC 8-1-AAC 8-13.

LOW, R. D. H., 1969: A Generalized Equation for the Solution Effect in Droplet Growth. *J. Atmos. Sci., 26*, 608–611.

MILBRANDT, J. A. and M. K. YAU, 2005: A Multimoment Bulk Microphysics Parameterization. Part II: A Proposed Three-Moment Closure and Scheme Description. *J. Atmos. Sci., 62*, 3065–3081.

OHTAKE, T. and P. J. HUFFMAN, 1969: Visual Range in Ice Fog. *J. Appl. Meteor., 8*, 499–501.

PRENNI, A. J., P. J. DEMOTT, D. C. ROGERS, S. M. KREIDENWEIS, G. M. MCFARQUHAR, G. ZHANG, and M. R. POELLOT, 2009: Ice nuclei characteristics from M-PACE and their relation to ice formation in clouds. *Tellus, 61*, 436–448.

PRENNI, A. J., P. J. DEMOTT, S. M. KREIDENWEIS, J. Y. HARRINGTON, A. AVRAMOV, J. VERLINDE, M. TJERNSTRÖM, C. N. LONG, and P. Q. OLSSON, 2007: Can Ice-Nucleating Aerosols Affect Arctic Seasonal Climate? *Bull. Amer. Meteor. Soc., 88*, 541–550.

PRUPPACHER, H. and J. KLETT, 1997: *Microphysics of cloud and precipitation*. Kluwer Academic, 955 pp.

ROGERS, R. R. and M. K. YAU, 1989: *A short course in cloud physics*. 3 ed. Butterworth-Heinemann, 290 pp.

SASSEN, K. and G. C. DODD, 1989: Haze Particle Nucleation Simulations in Cirrus Clouds, and Applications for Numerical and Lidar Studies. *J. Atmos. Sci., 46*, 3005–3014.

SCHMITT, C., M. STUEFER, A. HEYMSFIELD, and C. K. KIM, 2013: The microphysical properties of ice fog measured in urban environments of Interior Alaska. *J. Geophy. Res.*, VOL. *118*, 1–12, 2013 doi:10.1002/jgrd.50822.

SCHOENBERG FERRIER, B., 1994: A Double-Moment Multiple-Phase Four-Class Bulk Ice Scheme. Part I: Description. *J. Atmos. Sci., 51*, 249–280.

SHAW, G. E., 1983: On the Aerosol Particle Size Distribution Spectrum in Alaskan Air Mass Systems: Arctic Haze and Non-Haze Episodes. *J. Atmos. Sci., 40*, 1313–1320.

SHULSKI, M. and G. WENDLER, 2007: *The Climate of Alaska*. University of Alaska Press, 216 pp.

SKAMAROCK, W. C., and COAUTHOURS, 2008: A description of the Advanced Research WRF version 3. NCAR Tech. Note NCAR/TN-475 + STR, 113 pp.

STRAKA, J., 2009: *Cloud and Precipitation Microphysics: principles and parameterization*. Cambridge University Press, 392 pp.

THOMPSON, G., R. M. RASMUSSEN, and K. MANNING, 2004: Explicit forecasts of winter precipitation using an improved bulk microphysics scheme. Part I: Description and sensitivity analysis. *Mon. Wea. Rev., 132*, 519–542.

THOMPSON, G., P. R. FIELD, R. M. RASMUSSEN, and W. D. HALL, 2008: Explicit Forecasts of Winter Precipitation Using an Improved Bulk Microphysics Scheme. Part II: Implementation of a New Snow Parameterization. *Mon. Wea. Rev., 136*, 5095–5115.

THUMAN, W. C. and E. ROBINSON, 1954: STUDIES OF ALASKAN ICE-FOG PARTICLES. *J. of Meteor., 11*, 151–156.

WALKO, R. L., W. R. COTTON, M. P. MEYERS, and J. Y. HARRINGTON, 1995: New RAMS cloud microphysics parameterization part I: the single-moment scheme. *Atmos. Res., 38*, 29–62.

WELCH, R. M., M. G. RAVICHANDRAN, and S. K. COX, 1986: Prediction of Quasi-Periodic Oscillations in Radiation Fogs. Part I: Comparison of Simple Similarity Approaches. *J. Atmos. Sci., 43*, 633–651.

YOUNG, K. C., 1974: A Numerical Simulation of Wintertime, Orographic Precipitation: Part I. Description of Model Microphysics and Numerical Techniques. *J. Atmos. Sci., 31*, 1735–1748.

ZHOU, B., 2011: Introduction to A New Fog Diagnostic Scheme. NCEP Office Note 466.

ZHOU, B., and B. S. FERRIER, 2008: Asymptotic Analysis of Equilibrium in Radiation Fog. *J. Appl. Meteor. and Climat., 47*, 1704–1722.

(Received August 10, 2013, revised December 6, 2013, accepted December 21, 2013)